Article:
Soós, S., Korsós, M.B., Morgan, H. et al. (2022) On the differences in the periodic behavior of magnetic helicity flux in flaring active regions with and without X-class events. Astrophysical Journal, 925 (2). 129. ISSN: 0004-637X

https://doi.org/10.3847/1538-4357/ac4094

The Astrophysical Journal, 925:129 (12pp), 2022 February 1 https://doi.org/10.3847/1538-4357/ac4094

On the Differences in the Periodic Behavior of Magnetic Helicity Flux in Flaring Active Regions with and without X-class Events

Sz. Soós[1,2], M. B. Korsós[1,2,3], H. Morgan[3], and R. Erdélyi[1,2,4]
[1] Department of Astronomy, Eötvös Loránd University, Pázmány Péter sétány 1/A, H-1112 Budapest, Hungary; komabi@gmail.com
[2] Hungarian Solar Physics Foundation, Petőfi tér 3, H-5700 Gyula, Hungary
[3] Department of Physics, Aberystwyth University, Ceredigion, Cymru SY23 3BZ, UK
[4] Solar Physics & Space Plasma Research Center (SP2RC), School of Mathematics and Statistics, University of Sheffield, Hounsfield Road S3 7RH, UK
Received 2021 July 16; revised 2021 November 24; accepted 2021 December 4; published 2022 February 1

Abstract

Observational precursors of large solar flares provide a basis for future operational systems for forecasting. Here, we study the evolution of the normalized emergence (EM), shearing (SH), and total (T) magnetic helicity flux components for 14 flaring (with at least one X-class flare) and 14 nonflaring (<M5-class flares) active regions (ARs) using the Space-weather Helioseismic Magnetic Imager Active Region Patches vector magnetic field data. Each of the selected ARs contain a δ-type spot. The three helicity components of these ARs were analyzed using wavelet analysis. Localized peaks of the wavelet power spectrum (WPS) were identified and statistically investigated. We find that (i) the probability density function of the identified WPS peaks for all the EM/SH/T profiles can be fitted with a set of Gaussian functions centered at distinct periods between ∼3 and 20 hr. (ii) There is a noticeable difference in the distribution of periods found in the EM profiles between the flaring and nonflaring ARs, while no significant difference is found in the SH and T profiles. (iii) In flaring ARs, the distributions of the shorter EM/SH/T periods (<10 hr) split up into two groups after flares, while the longer periods (>10 hr) do not change. (iv) When the EM periodicity does not contain harmonics, the ARs do not host a large energetic flare. (v) Finally, significant power at long periods (∼20 hr) in the T and EM components may serve as a precursor for large energetic flares.

Unified Astronomy Thesaurus concepts: Solar activity (1475); Solar flares (1496); Sunspots (1653); Solar active regions (1974); Solar active region magnetic fields (1975); Space weather (2037)

Supporting material: animations

1. Introduction

The interaction of solar activity with Earth's atmosphere occurs through a complex series of events called Space Weather (SW). The energetic solar flares and coronal mass ejections (CMEs) have dominant roles in SW because they can disrupt human technology, e.g., the functioning of electric power grids, aviation, radio communication, global power spectra (GPS), and space-based facilities (Eastwood et al. 2017). For this reason, it is vital to further develop existing prediction capabilities through the identification of observable precursors of flares and CMEs (see Barnes et al. 2016; Leka et al. 2019; Kusano et al. 2020; Patsourakos et al. 2020; Ahmadzadeh et al. 2021; Georgoulis et al. 2021). Understanding the physical processes of flare and CME precursors is still a challenging task in solar physics research (Florios et al. 2018; Korsós et al. 2019, and references therein). The most intense solar eruptions originate from the magnetically most complex, and highly twisted δ-type active regions (ARs; Georgoulis et al. 2019; Toriumi & Wang 2019). We employ this working hypothesis, and focus on the observational property of magnetic helicity flux in δ-type ARs in this work.

The source of magnetic helicity lies below the photosphere, and can be derived from magnetogram observations of the photosphere. Certain properties of the helicity are thought to be promising parameters to describe the pre-flare states of ARs. This is, partially, because the magnetic helicity flux often has a strong gradient before the flare and CME occur (Elsasser 1956; Moon et al. 2002a, 2002b; Park et al. 2008, 2012; Smyrli et al. 2010). The magnetic helicity carries information about the complexity of the magnetic field topology, and is therefore linked to the free magnetic energy of ARs, and the occurrence of flares. Thus, diagnostics related to the magnetic helicity may be valuable for flare prediction (Pariat et al. 2017; Thalmann et al. 2019; Korsós et al. 2020).

Recently, Prior et al. (2020) showed that the multi-resolution wavelet decomposition is a useful tool to analyze the magnetic helicity. Based on their theoretical work, Korsós et al. (2020) investigated the dynamic evolution of emergence (EM), shearing (SH), and total (T) magnetic helicity flux terms using a wavelet analysis in the case of three flaring and three nonflaring ARs. They found a relationship between the oscillatory behavior of the three magnetic helicity flux components and the associated flare activities. Their conjecture was that the three helicity flux components have common period(s) before flare onset. In comparison, the nonflaring ARs did not exhibit such common periodicities.

To further test the conjecture of Korsós et al. (2020), this work extends their approach by applying a more extensive set of diagnostics on a larger number of ARs. In this work, we investigate 14 flaring and 14 nonflaring ARs, and apply additional statistical tests, e.g., the Kolmogorov–Smirnov (K-S) test and the Gaussian mixture model (GMM). The selection criteria of the studied 28 ARs are listed in Section 2. We describe the method for the derivation of the magnetic helicity

Table 1
Summary Table of the Studied 28 ARs

Flaring ARs		Nonflaring ARs	
NOAA Number	Largest Flare Intensity	NOAA Number	Largest Flare Intensity
AR 11158	X-class	AR 11271	C-class
AR 11166	X-class	AR 11281	C-class
AR 11283	X-class	AR 11363	C-class
AR 11429	X-class	AR 11465	C-class
AR 11430	X-class	AR 11542	M1.6-class
AR 11515	X-class	AR 11678	C-class
AR 11520	X-class	AR 11726	M1.0-class
AR 11890	X-class	AR 11785	C-class
AR 11944	X-class	AR 12104	C-class
AR 12017	X-class	AR 12108	C-class
AR 12158	X-class	AR 12175	C-class
AR 12192	X-class	AR 12280	C-class
AR 12297	X-class	AR 12645	C-class
AR 12673	X-class	AR 12740	C-class

Note. The flaring ARs hosted at least one X-class flare, while the nonflaring ARs produced flares below the M2.0-class. All selected ARs contain a complex δ-type spot.

components in Section 3. Finally, Section 4 presents our analysis and summarizes the main findings of our work.

2. Data

In this study, similar to Korsós et al. (2020), ARs that contain X-class flares will be called flaring ARs. While ARs that do not contain X-class flares are defined as nonflaring ARs. As in Korsós et al. (2020), a random sample of 14 flaring and 14 nonflaring ARs are selected based on the following criteria:

1. The angular distance of an AR from the central meridian is up to $\pm 60^{\circ}$, to obtain the best possible quality data (Bobra et al. 2014).
2. The AR must have a δ-spot configuration.
3. Flaring ARs must be the location of at least one X-class flare.
4. Nonflaring ARs should not be the host of flares larger than M5.
5. Nonflaring ARs cannot be associated with fast CMEs. Here, we define CMEs with speeds 750 km s^{-1} or higher as a fast CME.

The selected 28 ARs are listed in Table 1, along with the largest flare intensity during the time of observation. The nonflaring ARs host flares of intensity classes A, B, and C except AR 11542, which produced one M1.6 flare, and AR 11726, which produced one M1.0 flare. The M-class flare intensities are at the boundary of what is considered to be a truly energetic flare.

3. Calculation of the Magnetic Helicity Flux

Following Korsós et al. (2020), we determine the EM/SH/T helicity flux components, given by the terms of the equation (see, Berger 1984):

$$T \equiv \left.\frac{dH}{dt}\right|_S = 2\int_S (\boldsymbol{A}_p \cdot \boldsymbol{B}_h)\boldsymbol{v}_{\perp z} dS - 2\int_S (\boldsymbol{A}_p \cdot \boldsymbol{v}_{\perp h})\boldsymbol{B}_z dS, \quad (1)$$

where $\boldsymbol{A}_p$ is the vector potential of the potential magnetic field $\boldsymbol{B}_p$. $\boldsymbol{B}_h$, $\boldsymbol{B}_z$, $\boldsymbol{v}_{\perp h}$, and $\boldsymbol{v}_{\perp z}$ are the tangential and normal components of the magnetic field and the tangential and normal components of velocity, respectively. On the right-hand side of Equation (1), the first term comes from the twisted magnetic flux tubes emerging into the solar atmosphere or also submerging into the subsurface layer (EM component). The second term comes from the shearing and braiding of the field lines, which is caused by the tangential motions on the solar surface (SH component).

The helicity is estimated for each AR using the Space-weather Helioseismic and Magnetic Imager Active Region Patches vector magnetic field measurements (Bobra et al. 2014) with a cadence of 12 minutes (*hmi.sharp_cea_720s*). The data is rebinned spatially by a factor of 4 reduction in order to make the code run faster.

Additional constraints are applied to mitigate the artificial 12 and 24 hr periods of the Solar Dynamics Observatory/Helioseismic and Magnetic Imager (SDO/HMI) magnetogram measurements. Based on Smirnova et al. (2013), the strength of the magnetic field is capped at a maximum of $|\pm 2000|$ G. We also impose a minimum threshold of $|\pm 200|$ G, which is commonly used in the literature (Tziotziou et al. 2015).

After the data binning and the applied constraints, the photospheric plasma velocity is estimated by applying the Differential Affine Velocity Estimator for Vector Magnetograms (DAVE4VM) algorithm with a 19 pixel window (Schuck 2008). The vector potential $\boldsymbol{A}_p$ was derived by the multigrid MUDPACK software (Adams 1993), solving the relevant elliptic partial differential equations.

4. Analysis

The wavelet power spectrum (WPS) is applied to both original and smoothed time series of EM/SH/T. Similar to Korsós et al. (2020), the smoothed series are subject to a smoothing window of 24 hr that was subtracted from the original data in order to further reduce the 12 and 24 hr SDO artifact (Smirnova et al. 2013). Following Korsós et al. (2020), we employ the WPS algorithm of Torrence & Compo (1998), using the default Morlet wavelet. From the WPS, GPS are calculated through averaging the WPS over time. We identify significance in regions of the WPS based on a 1σ level, estimated using a white noise model and the standard deviation of the input signal.

In contrast with Korsós et al. (2020), here, we identify local maxima in the WPS by using an implementation of the zeroth dimensional persistent homology method (Huber 2021) from a Python package.[5] It is important to note that we sought for peaks for significance levels and not for power. These peaks are shown as cyan-colored triangles for the case of AR 11430 in Figure 1. Only significant peaks inside the cone of influence are considered. These peaks are recorded for all 28 ARs, for both the original and smoothed series of all three helicity flux components. As expected due to a consideration of the wavelet decomposition at different periods, there are larger numbers of peaks at shorter periods (between 1 and 10 hr) while only a few peaks are detected at longer periods.

[5] http://git.sthu.org/

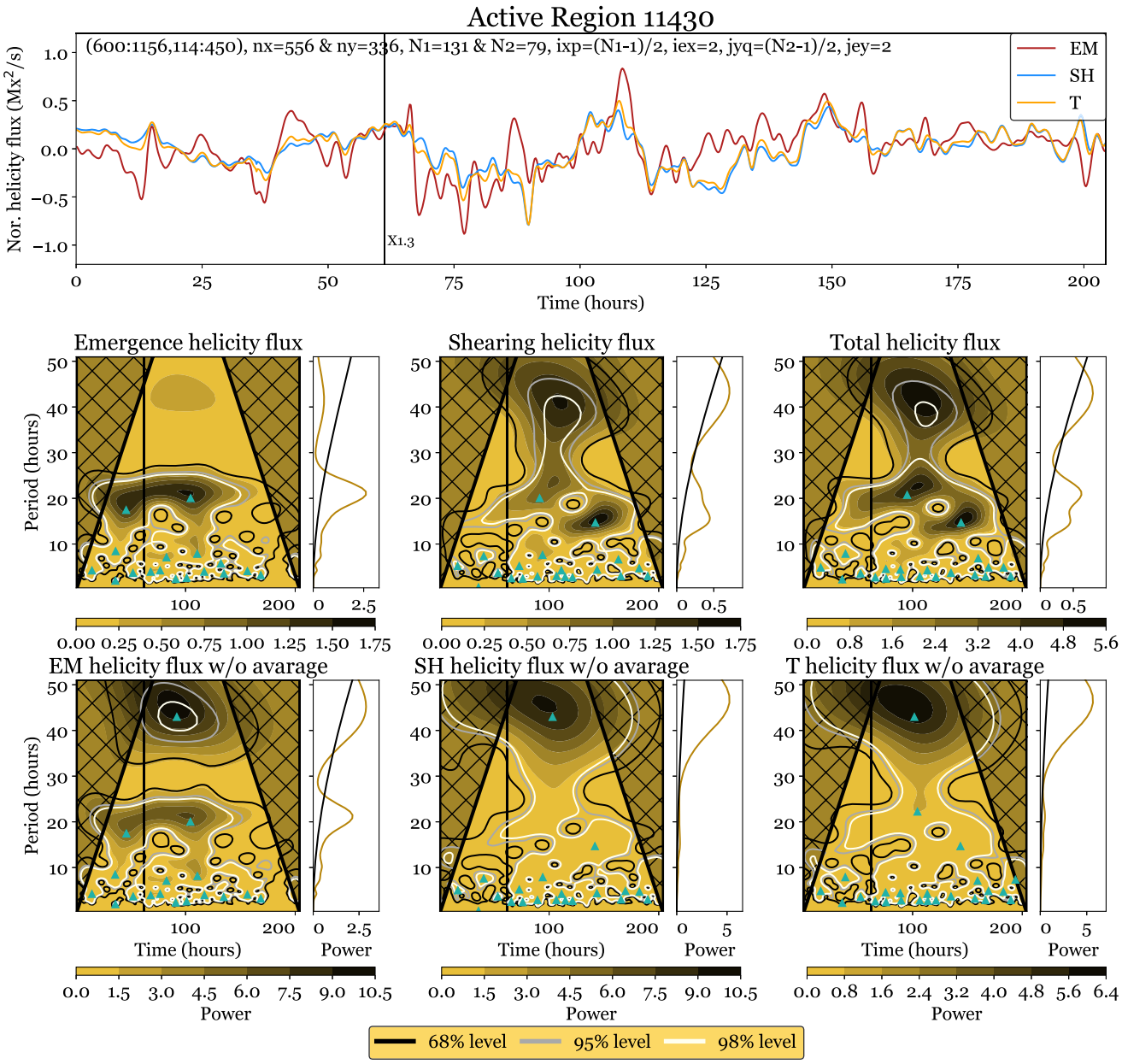

Figure 1. Wavelet analysis of the flaring AR 11430. Black vertical lines in all plots mark the onset time of the X1.3 flare. The top panel shows the unsmoothed EM/SH/T time series in red/blue/orange, respectively. The middle row panels display the WPS of the smoothed EM/SH/T helicity, while the bottom row panels depict the WPS of the unsmoothed time series. For each wavelet, the contour lines mark the significance levels (black at 68%, gray at 95%, and white at 98%), while the shaded color corresponds to the power, as shown in the color bars. In the WPS plots, the thick black lines bounding the gridded regions show the cone of influence, i.e., the domain where edge effects become important. Peaks of local maxima within significant regions, identified using a homology method (see text), are shown by the cyan-colored triangles. The plots to the right of each WPS are the GPS, or the time-averaged WPS.

4.1. Periodicity Distribution of Significant Peaks

The distribution of the identified WPS peaks are analyzed with a kernel density estimation (KDE) method. Figure 2 visualizes the KDE analysis of the smoothed EM/SH/T data and Figures 2(d)–(f) show the GMM results.

In particular, Figures 2(a)–(c) show the normalized probability density function (PDF) of the identified peaks as a function of periodicity. The PDF of flaring ARs are higher at shorter periods (0–10 hr) than the nonflaring ones for the EM (Figure 2(a)), and lower for the SH (Figure 2(b)). Based on Figure 2(a), the magnetic helicity flux EM indicates some level of differences for flaring versus nonflaring ARs, with $p = 0.547$. But, we also need to note that $p = 0.547$ is still large and not statistically significant to reject the null hypothesis that the flaring and nonflaring ARs have the same distribution of the WPS peaks. However, the distribution of the WPS peaks are the same in the case of SH and T, respectively, with the p-values of 0.852 and 0.944. The PDFs of Figures 2(a)–(c) show bands of preferred periodicities between (i) 2 and 9 hr, (ii) 11 and 14 hr, and (iii) 19 and 21 hr. We propose that these bands could indicate some global harmonic properties of the EM/SH/T fluxes. To test this hypothesis, a K-S test was performed to compare the peak distributions of flaring and nonflaring ARs, with the results summarized in Table 2.

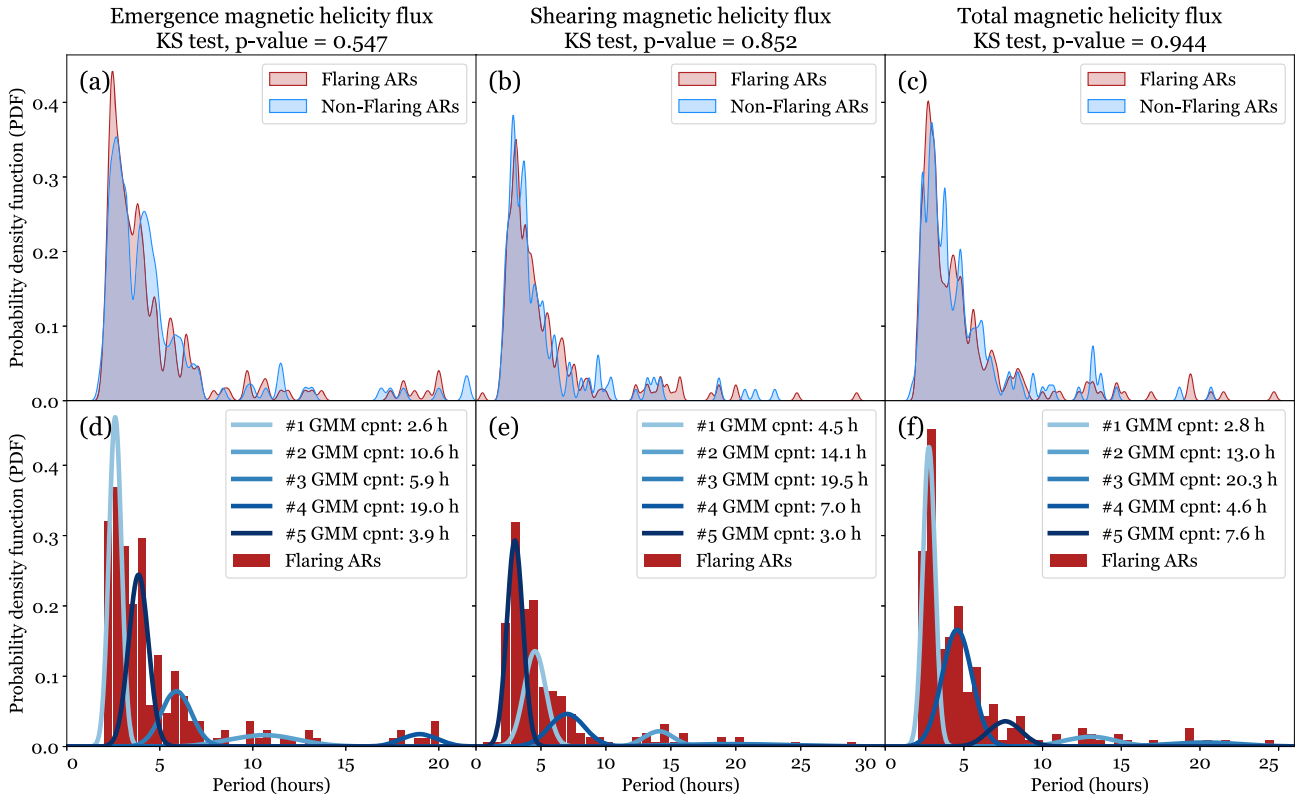

Figure 2. Top row: normalized PDF of the WPS peaks of flaring (red) and nonflaring (blue) ARs for (a) EM, (b) SH, and (c) T helicity, using KDE. Note these results are for the smoothed time series. Using GMM, panels (d)–(f) show the corresponding distributions fitted to a set of Gaussian functions. The number of Gaussian components are set to 5. The $1/n$ dependence refers to a power law, where $n = 1, 2, 3, ...$ is a positive integer, of the EM peaks of Gaussians is clearly visible in panel (d).

While performing the K-S analysis, our null hypothesis was that the similar periods are generated by the same driving mechanism for both flaring and nonflaring ARs. From Table 2, we see that all of the p-values are below 1σ, which means that the null hypothesis is true. At this stage, we do not know what exactly is the background driving mechanism for these oscillatory behaviors in the peak distributions of the three helicity fluxes. Therefore, since the null hypothesis is correct, we can assume that flaring and nonflaring ARs have the same global harmonic properties.

Let us next focus on the K-S test results of the T flux. It is not possible to distinguish between the two cases, namely, flaring versus nonflaring ARs. It is worth noting that there is almost no change in the outcome of the K-S test results applied to T flux whether using the original or smoothed data. On the other hand, the results of the K-S test of the SH (Figure 2(b)) and the EM (Figure 2(a)) fluxes do reveal different period bands in the flaring and nonflaring ARs.

4.2. Modeling the PDFs with GMM

Let us now fit the PDFs of the original and smoothed EM/SH/T fluxes, for the flaring and nonflaring cases, with Gaussians in order to reveal any regularity in the peak distributions. Namely, in Figures 2(d)–(f), the Gaussian fits are performed by employing the GMM. At first, the number of fitted Gaussian distributions were determined by the best Akaike information criterion (AIC) and Bayesian information criterion (BIC) values, which supported our earlier findings that the periods are aggregated in bands. The AIC/BIC analysis identified five components for the EM of flaring ARs, and only two or three components for the SH and T. In order to make a consistent comparison between all time series, and from visual inspection of Figures 2(d)–(f), we impose a set number of five GMM components for our analysis.

Table 2
K-S Test Results for Flaring versus Nonflaring AR Peaks

Helicity Flux	with Average		w/o Average	
	Statistic	p-value	Statistic	p-value
EM	0.086	0.547	0.048	0.991
SH	0.063	0.852	0.097	0.365
T	0.054	0.944	0.054	0.942

The central periodicities of the fitted GMM are summarized in Table 3. In each case, the fundamental frequency belongs to the largest period. Based on this fundamental frequency, we also calculated the expected higher harmonics, which are shown in square brackets in Table 3. In Figure 2(d) the $1/n$ dependence ($n = 1, 2, 3,\ldots$) of the GMM-fitted Gaussian peaks are, again, clearly visible, which may serve to be evidence for the presence of global eigenmodes.

Next, we investigate the relationship between the Gaussian central periods obtained by GMM of the flaring and nonflaring ARs. This relationship is visualized in Figure 3, where the x-axis shows the periods of flaring ARs while the y-axis is the periods of nonflaring ARs. The errors of the mean periods are estimated for the obtained periods using a bootstrap method,

Table 3
Magnetic Helicity Flux Periods Obtained with GMM (Five Components)

	Flaring ARs Harmonics	Nonflaring ARs with avg (hr)	w/o avg (hr)	with avg (hr)	w/o avg (hr)
	f	19.0 [19.0]	25.5 [25.5]	21.0 [21.0]	21.9 [21.9]
EM magnetic	p_1	10.6 [9.5]	19.5 [12.8]	17.5 [10.5]	17.8 [11.0]
	p_2	5.9 [6.3]	9.2 [8.5]	11.0 [7.0]	10.8 [7.3]
Helicity flux	p_3	3.9 [4.8]	4.9 [6.4]	4.5 [5.3]	4.5 [5.5]
	p_4	2.6 [3.8]	3.0 [5.1]	2.7 [4.2]	2.7 [4.4]
	f	19.5 [19.5]	20.7 [20.7]	20.5 [20.5]	18.7 [18.7]
SH magnetic	p_1	14.1 [9.8]	12.2 [10.4]	13.5 [10.3]	13.1 [9.4]
	p_2	7.0 [6.5]	5.8 [6.9]	9.2 [6.8]	9.1 [6.2]
Helicity flux	p_3	4.7 [4.9]	3.3 [5.2]	5.2 [5.1]	5.0 [4.7]
	p_4	3.0 [3.9]	0.5 [4.1]	3.1 [4.1]	3.1 [3.7]
	f	20.3 [20.3]	20.8 [20.8]	19.7 [19.7]	19.4 [19.4]
T magnetic	p_1	13.1 [10.2]	13.1 [10.4]	11.7 [9.9]	12.8 [9.7]
	p_2	7.2 [6.8]	7.7 [6.9]	6.1 [6.6]	8.7 [6.5]
Helicity flux	p_3	4.5 [5.1]	4.5 [5.2]	4.2 [4.9]	5.2 [4.9]
	p_4	2.8 [4.1]	2.8 [4.2]	2.8 [3.9]	3.1 [3.9]

Note. The mean values of the obtained (GMM) Gaussian distributions of the studied distributions are listed. Square brackets are the fundamental periods with the associated harmonics assuming the system is a uniform resonant waveguide.

using a random resampling repeated 10,000 times. In Figure 3, the black dashed line represents the 100% correlation between the flaring and nonflaring cases.

From Figure 3, we can see that the dependence of the EM clearly becomes deviated from that of the SH and T fluxes. Also, the mean periods of EM of the nonflaring ARs are longer than the flaring ones. These findings strongly suggest that the evolution of the EM flux component has a more prominent role in the flare-CME triggering processes when compared to that of the other two helicity flux components.

Previously, we determined the harmonics for each case of the period peaks of the oscillatory behavior of the various helicity flux components. From this, we can see that only the peaks appearing in the EM of flaring ARs are the ones that follow the properties of the harmonics well for an oscillatory waveguide system. The $1/n$ dependence ($n = 1, 2, 3, \ldots$) of the fitted Gaussians of EM of flaring ARs is evidence of such an oscillatory system (Figure 2(d)). Such a clear harmonic property is not detected in the different flux components of nonflaring ARs.

In summary, if the following series of events/features occur, during the evolution of an AR, these may alert us to an impending flare/CME:

1. Once a δ-spot is forming,
2. Where shorter periods appear in the EM,
3. Where these periods show the properties of harmonics of a resonant waveguide system.

4.3. Distribution of Peaks of Flaring ARs

We now investigate the periodicity distributions of peaks before and after the flares. In Figure 4(a), we plot the distribution of the localized WPS peaks of EM before (red) and after (blue) the largest intensity flares. Based on the K-S test with $p = 0.305$, the two distributions are different: after the flare, the main peak splits into two distinct peaks (~2.5 and ~4.5 hr).

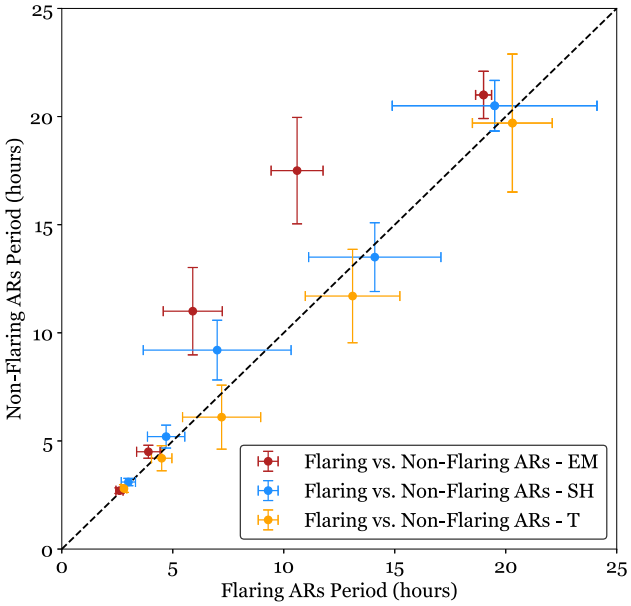

Figure 3. Correlation between the Gaussian central periods of flaring and nonflaring ARs. The error bars are estimated with a bootstrapping method. The dashed black line shows the one-to-one correspondence between flaring and nonflaring periodicities. Only the EM periodicities are significantly above this line.

In the SH case (Figure 4(b)), the K-S test with $p = 0.199$ indicates that the period distributions are different before and after the flare. The most striking feature here is, again, that the short periods split into two groups after the flare.

The T component behaves similarly to EM, as shown in Figure 4(c). The magnitudes of the periods shift toward lower values after the flare onset, and the higher periods mostly disappear. Likewise to EM, the K-S test result of p-value $= 0.370$ shows that the different period distributions before and after the flare are not as pronounced as in the SH case.

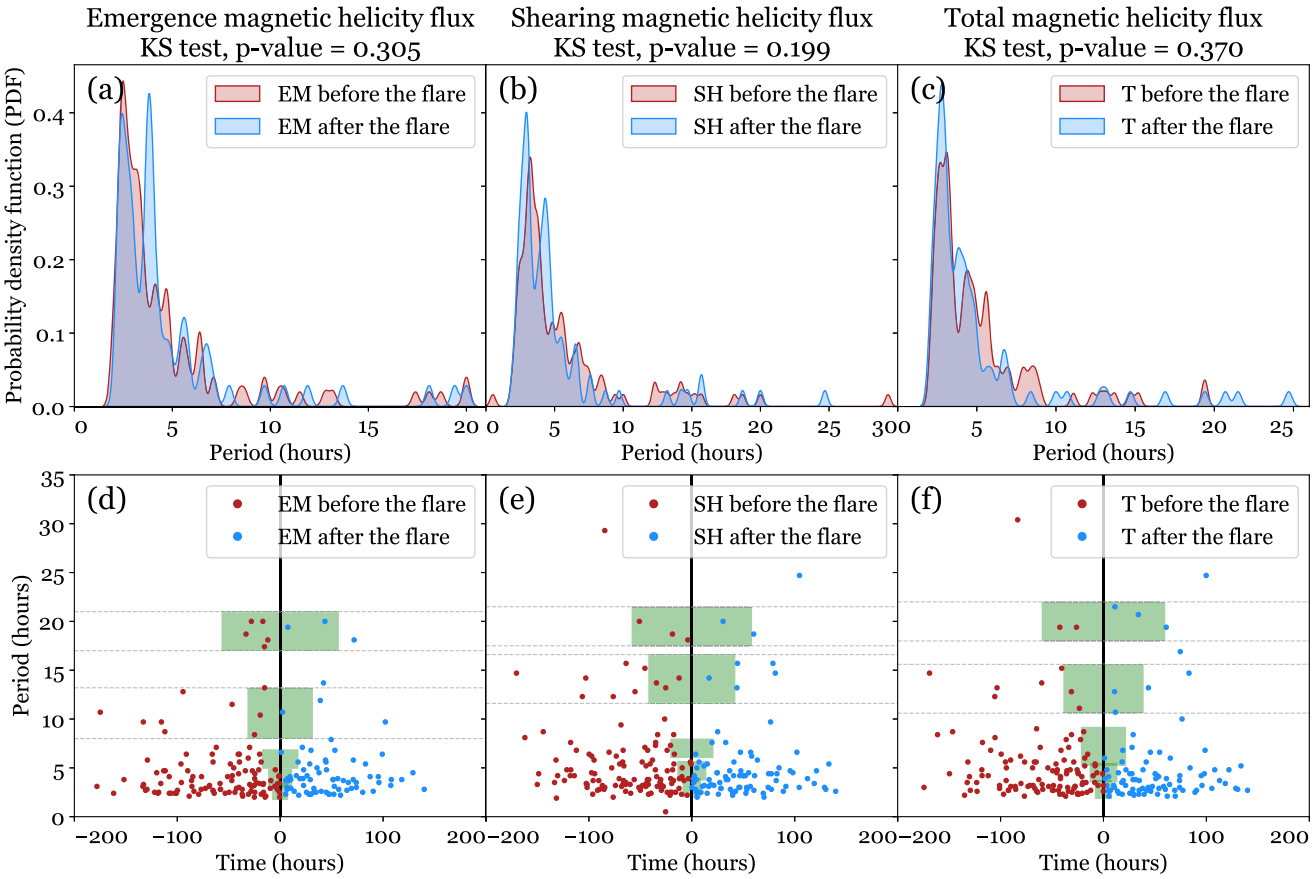

Figure 4. Panels (a)–(c): distribution of EM/SH/T peaks before (red) and after (blue) the flares. In the EM (a) case the most striking feature is that the short periods split into ∼2.5 and ∼4.5 hr after the flare occurred. Similar to the peaks of SH (b). Panels (d)–(f): EM/SH/T periods of all flaring ARs. The black vertical line marks the reference time of the flares. The center of the green rectangles is given by the center of the Gaussian distributions fitted by the GMM method. The height of the rectangles corresponds to the FWHM value of the Gaussians fitted by the GMM method. The width of the green rectangles corresponds to three periods. The gray dashed lines are the boundaries of green rectangles, in case of the longer periods of EM/SH/T.

Next, Figures 4(d)–(f) show the periodicities as a function of time relative to the onset time of the largest flare. In general, we find that shorter periods (2–8 hr) are continuously present. However, the peak of longer periods ($\geqslant$10 hr) are more often observed before or just a few hours after the flares. Interestingly, the peaks of the longer periods of EM/SH/T do not split up into further bands after the flares, as can be seen between the dashed lines in Figures 4(d)–(f).

In summary, the shorter periods (<10 hr) seem to separate into two groups after the flare (see Figures 4(a)–(c), while the longer periods do not (see Figures 4(d)–(f)).

4.4. Distribution of Peaks of Nonflaring ARs

Next, the peak distributions of nonflaring ARs are examined, separately for the EM/SH/T helicity fluxes. Since there is no set moment of flare onset time in this case, we select an arbitrary reference time in every nonflaring AR. Since the average investigated time interval of an AR was about 7–9 days in duration, we define a set of reference times ranging from 0–200 hr, in 5 hr increments (see the three corresponding animations for EM/SH/T in the online material). This range of about a total of 40 different reference times helps to avoid bias in the analysis. (*Note: Please find the animations in the Appendix.*)

For each arbitrarily chosen time, the distributions of EM/SH/T are analyzed. The studied time intervals (between 50 and 140 hr) give an appropriate distribution before and after the arbitrary time, because outside of these time intervals, the peaks sometimes run very high due to the normalization of the distribution. For this reason, we filter the animations and cut off the beginning and end of the arbitrarily chosen time intervals.

In summary, and most importantly, there is no significant change in the peak distribution before and after a suitably chosen (say 40–50 to 130–145 hr) arbitrary time when compared to the corresponding counterparts of the analyses of flaring ARs. Indeed, this is the expected behavior since there is no naturally distinguished physical reference time in nonflaring ARs when the conditions of helicity oscillations may undergo rapid changes, as occurs in flaring ARs. Overall, from the results found so far, we may safely conclude that there is an intrinsic relationship between the periodic oscillations of the helicity fluxes and the flaring activities of an AR.

4.5. Comparing the Number of Periods in ARs

In Figures 4(d)–(f), the periods of WPS peaks of all flaring ARs are plotted separately for the EM/SH/T fluxes. The black vertical lines represent the reference time of each flare event. The center of the green rectangles is determined by the center of the Gaussian distributions fitted by the GMM method (as seen in Table 3). The height of the rectangles corresponds to the FWHM value of the Gaussians, and the width of the rectangles corresponds to three whole periods. This indicative

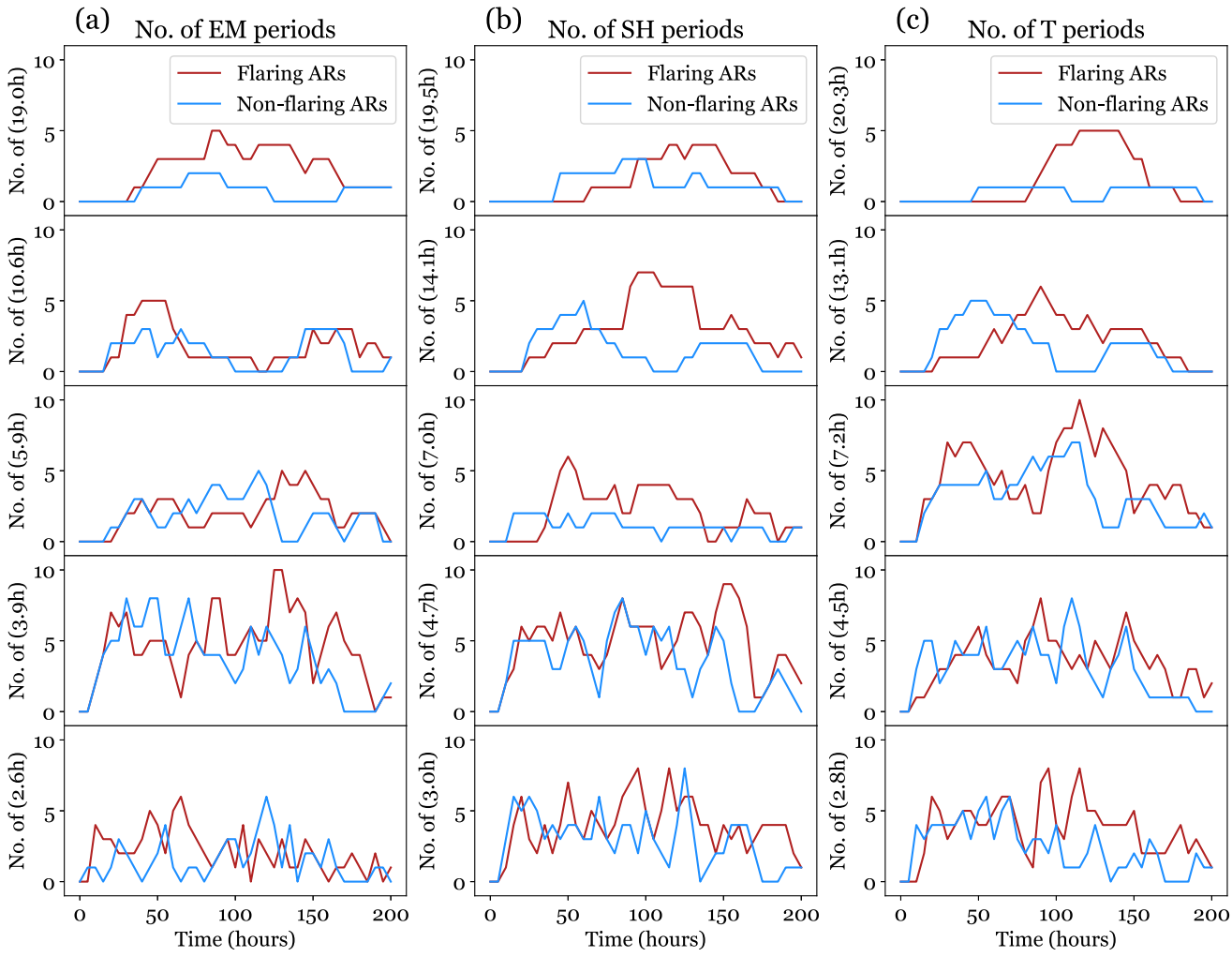

Figure 5. Number of (a) EM, (b) SH and (c) T oscillatory peak periods in flaring and nonflaring ARs. The blue/red lines correspond to nonflaring/flaring ARs. Long periods (∼20 hr) appear in the oscillatory peaks of the WPS of the T and EM fluxes of flaring ARs, which seem to be linked to flare/CME eruptions.

width is chosen because by multiplying the means of Gaussians by *e*-fold, one would have about three oscillatory periods.

We count the number of peaks appearing within each defined rectangular region for the flaring ARs, and for an interval three periods earlier of the arbitrarily chosen reference times for the nonflaring ARs. In Figure 5, we plot the number of points summed from each green rectangle as a function of the arbitrarily chosen reference times for the magnetic helicity flux components of flaring and nonflaring ARs. The *x*-axis of Figure 5 corresponds to the nonflaring ARs reference times ranging from 0–200 hr, in 5 hr increments. A total of 40 different reference times as in Section 4.4. For the EM case (Figure 5(a)), long (∼19 hr) periods are present throughout, and are significantly higher for the flaring ARs. For shorter periods, it is difficult to distinguish between flaring and nonflaring ARs. In the SH case (Figure 5(b)), the maximum count is clearly identifiable at ∼14.1 hr. For the flaring ARs, the long periods (∼20 hr) appear for the total helicity flux T (Figure 5(c)), from which we conclude that if these periods appear, we may expect flare/CME eruptions. No such clear difference can be established from the shorter periods. At the moment of ∼13.1 hr, the number of flaring periods is slightly higher than in the nonflaring case, but this alone is not sufficient to use it for flare warning.

The presence of long periods in EM and T suggests that it plays a crucial role in the formation of flares.

5. Summary

In this work, we tested and further developed the results found in Korsós et al. (2020), by carrying out wavelet analysis, about the dynamic evolution of EM/SH/T magnetic helicity flux terms. Korsós et al. (2020) reported a unique relationship between the oscillatory behavior of the three magnetic helicity flux components and the associated flare activities.

To test their conjecture, here, we have analyzed the EM/SH/T magnetic helicity flux evolution of 14 flaring and 14 nonflaring ARs. Following the methodology of Korsós et al. (2020), first we mitigated the artificial 12 and 24 hr periods of the SDO/HMI magnetogram measurements by setting lower |±200| G and upper |±2000| G magnetic field boundaries for an AR, based on Smirnova et al. (2013) and Tziotziou et al. (2015). To further reduce the 12 and 24 hr SDO artifacts, we

smoothed the time series of EM/SH/T with 24 hr smoothing window and subtracted the obtained averaging from the original data.

As a next step, we have constructed the WPS of EM/SH/T time series. Regions of the WPS at above the 1σ significance level were identified and the peaks contained in these regions were recorded. Before finalizing the $|\pm 200|$ G lower and $|\pm 2000|$ G upper boundaries, we also extensively looked into how these boundaries change the results when limiting the magnetic field strength. We found that, in general, if one caps the magnetic field strength, the lower (3–15 hr) periods become less frequent, as was suggested by Smirnova et al. (2013).

After determining the lower and upper magnetic field boundary values, the following results were found by means of statistical analysis (for more details see Section 4) of the identified local peaks within 1σ significance level of the corresponding WPS:

1. For flaring and nonflaring ARs, the EM/SH/T periodicities occur in bands. These bands are between (i) 2 and 9 hr, (ii) 11 and 14 hr, and (iii) 19 and 21 hr (see Figures 2(d)–(f)).
2. The distribution of EM/SH/T peak periodicities were fitted using a GMM. Figure 2(d) shows the $1/n$ dependence ($n = 1, 2, 3, ...$, a positive integer) of the GMM-fitted EM peaks for flaring ARs. However, such clear harmonic oscillatory properties were not present in the SH/T flux components of flaring and in the EM/SH/T fluxes of nonflaring ARs.
3. There is a noticeable difference in the distribution of central periods found in the EM profiles between the flaring and nonflaring ARs, while no significant difference is found in the cases of the SH and T profiles. The central periodicities of the nonflaring EM are significantly longer than the flaring.
4. For the three helicity components, the distribution of lower periods (<10 hr) are concentrated around $\sim$2.5 hr before the flare events, see Figures 4(a)–(c). Interestingly, these lower periods are separated into two groups (i.e., $\sim$2.5 and $\sim$4 hr), after the flares (see Figures 4(a)–(c)). This could be explained by the rearrangement and disappearance of the magnetic field as a waveguide resonator *allowing* oscillations around only $\sim$2.5 hr prior to flaring. However, the distribution of the longer periods (>10 hr) does not change after the flares, see the highlighted areas with dashed lines in Figures 4(d)–(f).
5. In the flaring AR cases, the stronger presence of long periods in the EM (i.e., $\sim$19 hr) and in T ($\sim$20 hr) oscillatory data would suggest that the EM component does play a more crucial role in the formation of flares (see Figure 5). This condition is only indicative as these periods may also appear in few cases of nonflaring ARs (see the top panels in columns (a) and (c) of Figure 5).
6. In the nonflaring ARs studied, there is no significant change in the peak distributions before and after a suitably chosen (say 40–50 to 130–145 hr) arbitrary reference time when compared to the counterpart distributions before and after in flaring ARs (see Figures A1–A3).
7. To test the robustness of our findings, we look for a bias in the selection of AR samples in two ways: (i) we exclude a random AR from the 14 flaring AR samples, as well as one from the 14 nonflaring AR samples; and (ii) we generate synthetic samples using bootstrap method, then we reconstruct Figures 2–5 again. In both cases we came to the same conclusion that neither the synthetic samples nor the exclusion of 1–1 ARs change the results significantly.

Based on the above, we conclude that there is an intrinsic relationship between the periodic oscillations of the helicity fluxes and flare activity. Our results show that the evolution of the EM helicity flux component has a more prominent role in the flare-CME triggering process, especially when

1. The AR has a δ-spot.
2. Shorter oscillatory periods appear in the EM flux data.
3. These periods show the presence of a harmonic oscillatory resonator.

To apply these results as a precursor, or, use them to distinguishing between flaring and nonflaring ARs, we need at least $\sim$2.5 days data to study the evolution of the three helicity flux components and reveal the possible characteristic long period(s) of a flaring AR by wavelet analyses.

The authors thank the referee and the handling editor for their constructive comments that have improved the paper. M.B.K. and H.M. are grateful to the Science and Technology Facilities Council (STFC), (UK, Aberystwyth University, grant No. ST/S000518/1), for the support received while carrying out this research. R.E. is grateful to STFC (UK, grant No. ST/M000826/1) and EU H2020 (SOLARNET, grant No. 158538). R.E. also acknowledges support from the Chinese Academy of Sciences President's International Fellowship Initiative (PIFI, grant No. 2019VMA0052) and The Royal Society (grant No. IE161153). The authors also acknowledge the support received from OTKA (grant nr K128384), Hungary.

Software: MUDPACK (Adams 1993), Wavelet Analysis (Torrence & Compo 1998), Persistent Homology (Huber 2021), seaborn (Waskom 2021), sklearn (Pedregosa et al. 2011), scipy (Virtanen et al. 2020).

Appendix

Here, we list the associated animations of the distribution of peaks of nonflaring ARs, available in the online version. The animations show the distribution of periods before the arbitrarily chosen reference moment of time (in blue) and the distribution of periods after the arbitrarily chosen reference time (in red). See Figures A1, A2, and A3 for nonflaring EM, SH, and T animations.

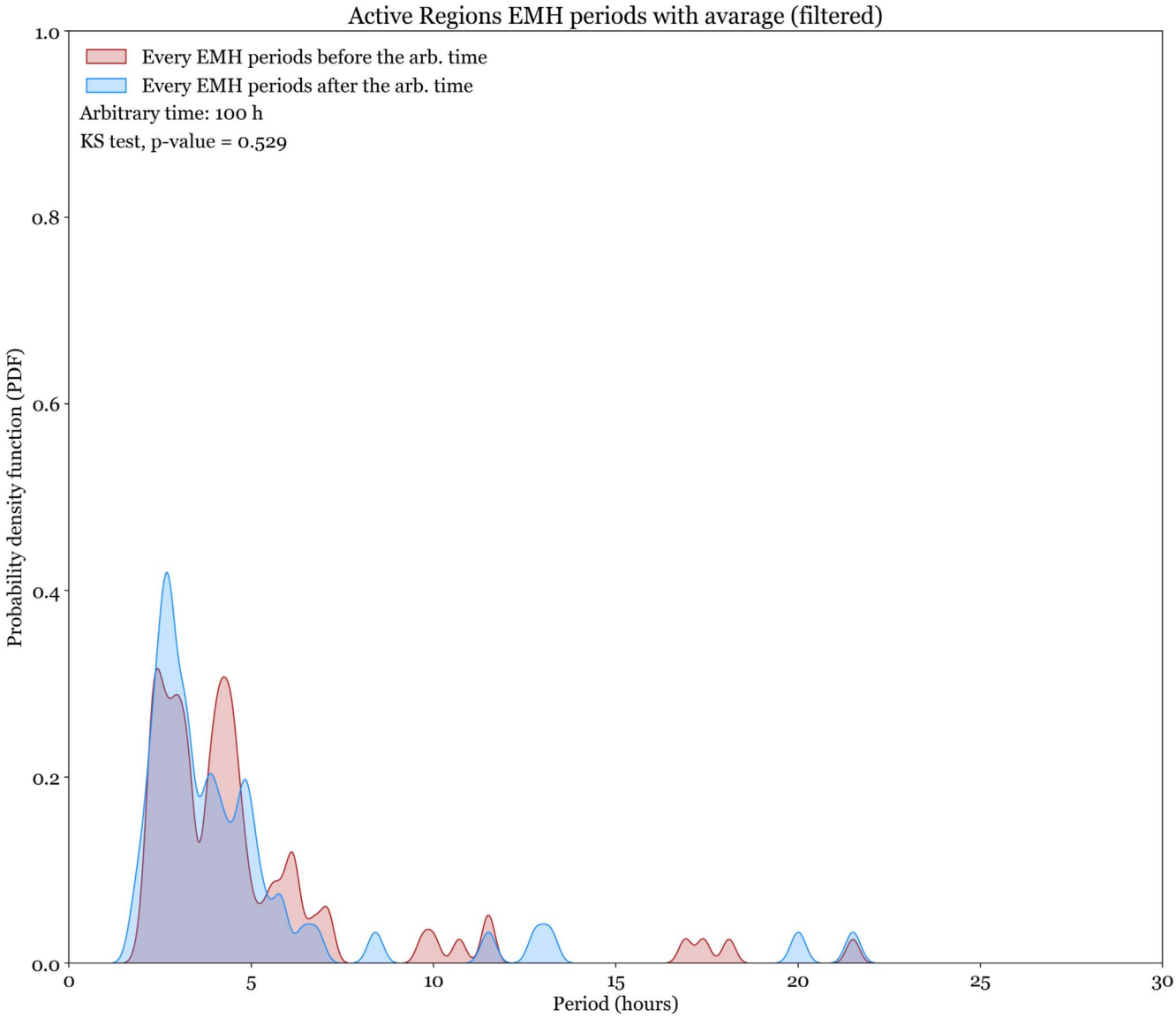

Figure A1. This figure is available as an animation, which shows consecutive reference times of nonflaring EM before/after the chosen reference time. Only small fluctuations are visible. The animation runs between arbitrary times 40–140 hr. The real-time duration of the animation is 2 s.

(An animation of this figure is available.)

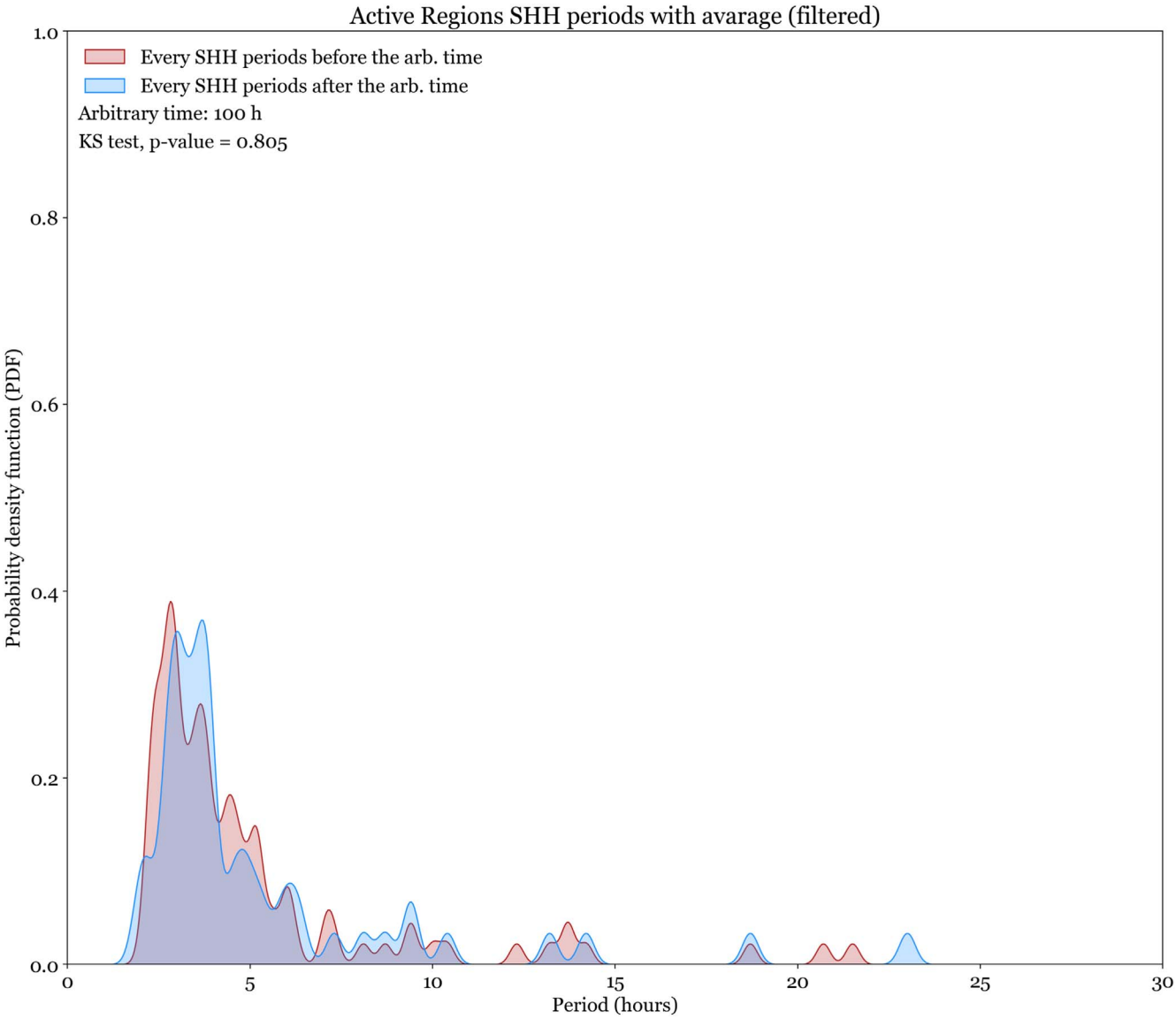

Figure A2. This figure is available as an animation, which shows consecutive reference times of nonflaring SH before/after the chosen reference time. Only small fluctuations are visible. The animation runs between arbitrary times 45–130 hr. The real-time duration of the animation is 2 s.

(An animation of this figure is available.)

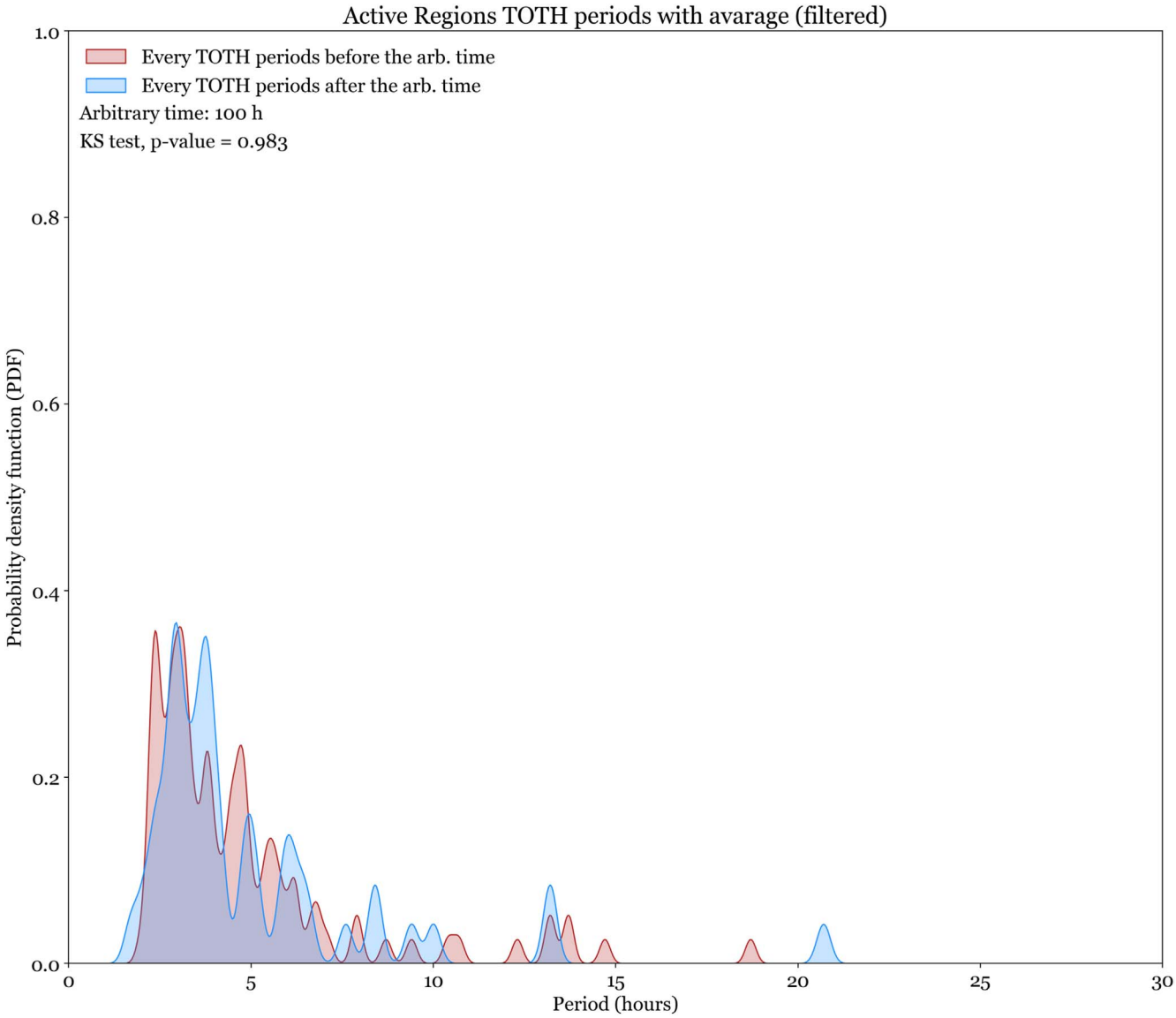

Figure A3. This figure is available as an animation, which shows consecutive reference times of nonflaring T before/after the chosen reference time. Only small fluctuations are visible. The animation runs between arbitrary times 50–125 hr. The real-time duration of the animation is 2 s.

(An animation of this figure is available.)

ORCID iDs

Sz. Soós https://orcid.org/0000-0002-3606-161X
M. B. Korsós https://orcid.org/0000-0002-0049-4798
H. Morgan https://orcid.org/0000-0002-6547-5838
R. Erdélyi https://orcid.org/0000-0003-3439-4127

References

Adams, J. C. 1993, ApMaC, 53, 235
Ahmadzadeh, A., Aydin, B., Georgoulis, M. K., et al. 2021, ApJS, 254, 23
Barnes, G., Leka, K. D., Schrijver, C. J., et al. 2016, ApJ, 829, 89
Berger, M. A. 1984, GApFD, 30, 79
Bobra, M. G., Sun, X., Hoeksema, J. T., et al. 2014, SoPh, 289, 3549
Eastwood, J. P., Biffis, E., Hapgood, M. A., et al. 2017, Risk Anal., 37, 206
Elsasser, W. M. 1956, AmJPh, 24, 85
Florios, K., Kontogiannis, I., Park, S.-H., et al. 2018, SoPh, 293, 28
Georgoulis, M. K., Bloomfield, D. S., Piana, M., et al. 2021, JSWSC, 11, 39
Georgoulis, M. K., Nindos, A., & Zhang, H. 2019, RSPTA, 377, 20180094
Huber, S. 2021, in Data Science—Analytics and Applications, ed. P. Haber et al. (Berlin: Springer), 81
Korsós, M. B., Romano, P., Morgan, H., et al. 2020, ApJL, 897, L23
Korsós, M. B., Yang, S., Erdélyi, R., et al. 2019, JSWSC, 9, A6
Kusano, K., Iju, T., Bamba, Y., & Inoue, S. 2020, Sci, 369, 587
Leka, K. D., Park, S.-H., Kusano, K., et al. 2019, ApJS, 243, 36
Moon, Y.-J., Chae, J., Choe, G. S., et al. 2002a, ApJ, 574, 1066
Moon, Y.-J., Choe, G. S., Wang, H., et al. 2002b, ApJ, 581, 694
Pariat, E., Leake, J. E., Valori, G., et al. 2017, A&A, 601, A125
Park, S.-H., Cho, K.-S., Bong, S.-C., et al. 2012, ApJ, 750, 48
Park, S.-H., Lee, J., Choe, G. S., et al. 2008, ApJ, 686, 1397
Patsourakos, S., Vourlidas, A., Török, T., et al. 2020, SSRv, 216, 131
Pedregosa, F., Varoquaux, G., Gramfort, A., et al. 2011, J. Mach. Learn. Res., 12, 2825
Prior, C., Hawkes, G., & Berger, M. A. 2020, A&A, 635, A95
Schuck, P. W. 2008, AGUFM, 2008, SH51A
Smirnova, V., Efremov, V. I., Parfinenko, L. D., Riehokainen, A., & Solov'ev, A. A. 2013, A&A, 554, A121
Smyrli, A., Zuccarello, F., Romano, P., et al. 2010, A&A, 521, A56
Thalmann, J. K., Moraitis, K., Linan, L., et al. 2019, ApJ, 887, 64
Toriumi, S., & Wang, H. 2019, LRSP, 16, 3
Torrence, C., & Compo, G. P. 1998, BAMS, 79, 61
Tziotziou, K., Park, S. H., Tsiropoula, G., & Kontogiannis, I. 2015, A&A, 581, A61
Virtanen, P., Gommers, R., Oliphant, T. E., et al. 2020, NatMe, 17, 261
Waskom, M. L. 2021, JOSS, 6, 3021